Adjoint-Based Aerodynamic Design on Unstructured Meshes

Enrico Fabiano [*], Dimitri Mavriplis [†]

Department of Mechanical Engineering,University of Wyoming, Laramie, WY 82071-3295.

This work presents initial optimization results for the Aerodynamic Design Optimization Discussion Group Cases 1 and 3 on unstructured meshes. A sequential quadratic programming algorithm is used to drive the constrained optimizations and the objective and constraint functional sensitivities are computed with the discrete adjoint method. After introducing the aerodynamic flow solvers employed, optimization results are discussed. The two dimensional optimization delivers an optimal solution, but yields higher drag values than other participants, most likely due to the airfoil parameterization employed in this work. The three dimensional optimization converges to a feasible optimum and is in good agreement with the workshop results.

I. Introduction

The use of Computational Fluid Dynamics (CFD) based design is now everyday practice in the aerospace community thanks to its quick turn-around time, especially for steady-state design conditions. Through the application of optimal shape modification, aerodynamic shape optimization is often used together with computational fluid dynamics to meet unique performance requirements. The use of shape optimization techniques is now fairly well established in the aircraft industry, where two-dimensional airfoil optimization techniques have seen widespread use since their initial appearances decades ago.[1] The need to solve ever more challenging design optimization problems characterized by extreme flow conditions that need to be finely resolved and the large and rich design spaces typically associated with aerodynamic design makes gradient based optimization techniques a valuable optimization tool. In the context of gradient based optimization adjoint techniques have played a major role since the full sensitivity vector of a single objective with respect to any number of design variables can be computed with a single adjoint solution, at a cost roughly equivalent to a single flow solution.[2,3]

In this paper we present initial gradient-based optimization results for the benchmark optimization problems 1 and 3 from the AIAA Aerodynamic Design Optimization Discussion Group on unstructured meshes with a discrete adjoint methodology.[4]

The first optimization considered, ADODG problem 1, deals with the two dimensional inviscid drag minimization of a modified NACA 0012 airfoil under a thickness constraint. The second optimization case considered, ADODG problem 3, deals with the twist optimization of a rectangular wing in subsonic inviscid flow subject to a lift constraint. The paper is structured as follows: section II introduces the two flow solvers used in this works and the discrete adjoint sensitivity approach, section III discusses optimization results from ADODG problems 1 and 3 and section IV draws conclusions and highlights future work.

II. Aerodynamic Analysis and Sensitivity Formulation

II.A. Flow Solver Analysis Formulation

Two different flow solvers have been used in this work. An in-house 2D Euler solver and the NSU3D[5] unstructured mesh Reynolds-averaged Navier-Stokes solver. Both solvers have been validated for steady-state and time-dependent flows and they are augmented with a discrete tangent and adjoint sensitivity capability. Since all the optimization cases considered here assume inviscid flow, a brief description of the flow solvers is given only regarding the Euler equations.

The flow solvers are based on the conservative form of the Euler equations which may be written as

$$\frac{\partial \mathbf{U}(\mathbf{x},t)}{\partial t} + \nabla \cdot \mathbf{F}(\mathbf{U}) = 0 \tag{1}$$

---

[*]PhD candidate; efabiano@uwyo.edu
[†]Professor; mavripl@uwyo.edu

American Institute of Aeronautics and Astronautics

where the state vector $\mathbf{U}$ consists of the conserved variables in the Euler equations and the flux vector $\mathbf{F} = \mathbf{F}(\mathbf{U})$ contains the inviscid flux. The equations are closed with the perfect gas equation of state. The solvers use a second order accurate formulation where the inviscid flux integral around a closed control volume is discretized as:

$$\mathbf{R}(\mathbf{U}) = \int_{dB} [\mathbf{F}(\mathbf{U})] \cdot \mathbf{n} dB = \sum_{i=1}^{n_{edge}} \mathbf{F}_{e_i}^{\perp}(\mathbf{U}, \mathbf{n}_{ei}) B_{e_i} = 0 \qquad (2)$$

where B_e is the edge length, $\mathbf{n}_e$ is the unit normal of the edge, and $F_e^{\perp}$ is the normal flux across the edge. The normal flux across the edge is computed using the second-order accurate matrix dissipation scheme[6] as the sum of a central difference and an artificial dissipation. For the case of steady-state flows considered in this work, the time derivative term in equation (1) represents a pseudo-time term used to facilitate convergence to the steady state solution. After the residual vector $\mathbf{R}$ is linearized with respect to the unknown flow solution vector $\mathbf{w}$, the system of nonlinear equations (2) is solved for using Newton's method as:

$$\left[\frac{\partial \mathbf{R}^k}{\partial \mathbf{U}^k} \right] \delta \mathbf{U}^k = -\mathbf{R}^k \qquad (3)$$
$$\mathbf{U}^{k+1} = \mathbf{U}^k + \delta \mathbf{U}^k$$
$$\delta \mathbf{U}^k \to 0, \mathbf{U}^n = \mathbf{U}^k$$

The above system of equations is solved in 2D using a GMRES Krylov solver preconditioned with a colored Gauss Seidel strategy, and in 3D with a non-linear multigrid algorithm.

II.B.   Mesh deformation capability

In order to apply the optimal shape changes given by the optimization algorithm a mesh deformation strategy must be employed. For the two dimensional case a spring analogy approach is implemented where the mesh is seen as a network of interconnected springs whose coefficients are assumed to be inversely proportional to the second power of the edge length. Two independent force balance equations are formulated for each node in response to the surface displacements. The resulting system of equations is solved using a GMRES Krylov solver preconditioned with a Jacobi algorithm, similar to the solution strategy for the flow. For the three dimensional optimization case a linear elastic analogy mesh deformation approach has been used. In this approach, the mesh is modelled as a linear elastic solid with a variable modulus of elasticity that can be prescribed either as inversely proportional to cell volume or to the distance of each cell from the nearest wall.[7, 8] The resulting equations are discretized and solved on the mesh in its original undeformed configuration in response to surface displacements using a line-implicit multigrid algorithm analogous to that used for the flow equations. In both cases the governing equations for the mesh deformation can be written symbolically as:

$$\mathbf{G}(\mathbf{x}, \mathbf{x_{surf}}(\mathbf{D})) = \mathbf{0} \qquad (4)$$

where $\mathbf{x}$ denotes the interior mesh coordinates and $\mathbf{x_{surf}}(\mathbf{D})$ are the surface mesh coordinates that depend on the shape parameters that define the surface geometry.

II.C.   Aerodynamic Sensitivity Analysis Formulation

The basic sensitivity analysis implementation follows the strategy developed in references.[4, 9] Consider an arbitrary objective function L that is evaluated using the steady flow solution $\mathbf{U}$ and steady mesh solution $\mathbf{x}$ expressed as:

$$L = L(\mathbf{U}, \mathbf{x}) \qquad (5)$$

Assuming that the state variables (i.e. $\mathbf{U}, \mathbf{x}$) are dependent on some input design parameters $\mathbf{D}$, the total sensitivity of the objective function L to the set of design inputs can be expressed as the inner product between the vector of state sensitivities to design inputs and the vector of objective sensitivities to the state variables as:

$$\frac{dL}{d\mathbf{D}} = \left[\begin{array}{cc} \frac{\partial L}{\partial \mathbf{x}} & \frac{\partial L}{\partial \mathbf{U}} \end{array} \right] \left[\begin{array}{c} \frac{\partial \mathbf{x}}{\partial \mathbf{D}} \\ \\ \frac{\partial \mathbf{U}}{\partial \mathbf{D}} \end{array} \right] \qquad (6)$$

American Institute of Aeronautics and Astronautics

The non-linear flow residual operator and the mesh residual operator as described earlier provide the constraints which can be expressed in general form over the whole domains as:

$$\mathbf{G}(\mathbf{x}, \mathbf{D}) = 0$$
$$\mathbf{R}(\mathbf{U}, \mathbf{x}) = 0 \tag{7}$$

which when linearized with respect to the design inputs yields:

$$
\begin{bmatrix}
\dfrac{\partial \mathbf{G}}{\partial \mathbf{x}} & 0 \\[2ex]
\dfrac{\partial \mathbf{R}}{\partial \mathbf{x}} & \dfrac{\partial \mathbf{R}}{\partial \mathbf{U}}
\end{bmatrix}
\begin{bmatrix}
\dfrac{\partial \mathbf{x}}{\partial \mathbf{D}} \\[2ex]
\dfrac{\partial \mathbf{U}}{\partial \mathbf{D}}
\end{bmatrix}
=
\begin{bmatrix}
-\dfrac{\partial \mathbf{G}}{\partial \mathbf{D}} \\[2ex]
0
\end{bmatrix}
\tag{8}
$$

These constitute the forward sensitivity or tangent sensitivity equations. The mesh and flow sensitivity vectors can then be substituted into equation (6) to obtain the complete sensitivity of the objective with respect to the design variable $\mathbf{D}$. The forward sensitivity approach requires a new solution of equation (8) for each design parameter $\mathbf{D}$. On the other hand, the adjoint approach can obtain the sensitivities for any number of design inputs $\mathbf{D}$ at a cost which is approximately independent of the number of design variables. The adjoint problem can be obtained by pre-multiplying equation (8) by the inverse of the large coupled matrix and substituting the resulting expression for the sensitivities into equation (6) and defining adjoint variables as the solution of the system:

$$
\begin{bmatrix}
\dfrac{\partial \mathbf{G}}{\partial \mathbf{x}}^T & \dfrac{\partial \mathbf{R}}{\partial \mathbf{x}}^T \\[2ex]
0 & \dfrac{\partial \mathbf{R}}{\partial \mathbf{U}}^T
\end{bmatrix}
\begin{bmatrix}
\Lambda_{\mathbf{x}} \\[2ex]
\Lambda_{\mathbf{U}}
\end{bmatrix}
=
\begin{bmatrix}
\dfrac{\partial L}{\partial \mathbf{x}}^T \\[2ex]
\dfrac{\partial L}{\partial \mathbf{U}}^T
\end{bmatrix}
\tag{9}
$$

where $\Lambda_{\mathbf{U}}$ and $\Lambda_{\mathbf{x}}$ are the flow and mesh adjoint variables respectively. The final objective sensitivities can be obtained as:

$$
\frac{dL}{d\mathbf{D}}^T =
\begin{bmatrix}
\dfrac{\partial \mathbf{G}}{\partial \mathbf{D}}^T & 0
\end{bmatrix}
\begin{bmatrix}
\Lambda_{\mathbf{x}} \\[2ex]
\Lambda_{\mathbf{u}}
\end{bmatrix}
\tag{10}
$$

A more detailed description of the complete formulation is given in.[4]

III.   Optimization results

We present here the optimization results for the AIAA ADODG Case 1 and Case 3. The discrete adjoint method described in section II.C provides the objective and constraint functional sensitivities used to drive the SNOPT[10] sequential quadratic programming optimization algorithm.

III.A.   Case 1: Shape optimization of the modified NACA-0012 airfoil

The goal of this optimization is to reduce the drag of a modified NACA 0012[11] airfoil under a thickness constraint as described in equation (11)

$$min\ C_D$$
$$\texttt{subject to}$$
$$y \geq y_{baseline}\ \forall x \in [0,1] \tag{11}$$
$$w.r.t.\ \mathbf{D}$$

where $\mathbf{D}$ is the vector of design variables used for this optimization. The geometry is parameterized using the Class function - Shape function Transformation technique.[12] This parameterization technique gives an equation for the upper and lower surface of the airfoil as

$$y_{upper}(x) = C(x)Su(x) + x\Delta y_{upper} \tag{12}$$
$$y_{lower}(x) = C(x)Sl(x) + x\Delta y_{lower}$$

American Institute of Aeronautics and Astronautics

for a unit chord airfoil. $C(x)$ is the class function, that for an airfoil is

$$C(x) = \sqrt{x}(1-x) \tag{13}$$

and $\Delta y = \Delta y_{upper} + \Delta y_{lower}$ is the airfoil thickness at the airfoil trailing edge, which in this work is set to zero. $Sl(x)$ is the lower surface shape function defined as

$$Sl(x) = \sum_{i=1}^{N} Al_i S_i(x) \tag{14}$$

while $Su(x)$ is the upper surface shape function defined as

$$Su(x) = \sum_{i=1}^{N} Au_i S_i(x) \tag{15}$$

In equations (14) and (15) N is the order of the Bernstein polynomial used to describe the airfoil surface and the terms Au_i and Al_i are the ith design parameter on the upper and lower surface respectively used to scale the ith $S_i(x)$ term in the Bernestein polynomial defined in equation (16).

$$BPn = \sum_{i=1}^{N} S_i(x)$$
$$S_i(x) = \frac{N!}{i!\,(N-i)!}\, x^i\,(1-x)^{N-1} \tag{16}$$

Bernstein polynomials of order ten have been implemented in this work. To enforce geometrical symmetry only the ten lower surface coefficients Al_i are used as design variables, and the upper surface coefficients are determined as $Au_i = -Al_i$. The design variables Au_i and Al_i for the baseline airfoil have been determined with a non-linear least square fit to the NACA-0012mod[11] airfoil coordinates.

The flow around the airfoil is assumed to be inviscid and the far-field boundary condition is placed 20 chords away from the airfoil. The freestream Mach number is $M = 0.85$ and the angle of attack is zero. The flow solution and the adjoint are converged to machine precision and one design cycle for this optimization consists of one flow solution and one drag-adjoint solution. Because of equations (12), (14) and (15) the thickness constraint in equation (11) can be specified as a linear constraint as

$$Al_i \geq Al_{i_{base}} \quad i = 1, 10 \tag{17}$$

A mesh convergence study for the baseline airfoil is shown in Figure 1(a) highlighting the second order accuracy of the 2D flow solver. Each mesh in Figure 1(a) is generated by uniform refinement of the baseline mesh consisting of approximately 25,000 elements. The optimization is then carried out on the first uniformly refined mesh consisting of approximately 100,000 elements. The drag difference between the mesh employed in the optimization and the next refined one is $\Delta C_D \approx 0.56$ counts.

Optimization convergence is shown in Figure 2. Optimality is reduced more than 3 orders of magnitude after 15 nonlinear iterations and full convergence is reached after 36 iterations. The baseline and optimized drag coefficients are shown in Table 1 where it can be seen that the optimized airfoil has 196 drag-counts less than the baseline airfoil. This drag reduction is achieved by significantly increasing the thickness of the aft part of the airfoil, as shown in Figure 3 and Figure 3(a) shows that the thickness constraint has been satisfied everywhere along the chord.

Table 1. **Baseline and optimized drag coefficients (1 drag count = 1e4).**

	Drag counts
Baseline	466.96
Optimized	297.02

American Institute of Aeronautics and Astronautics
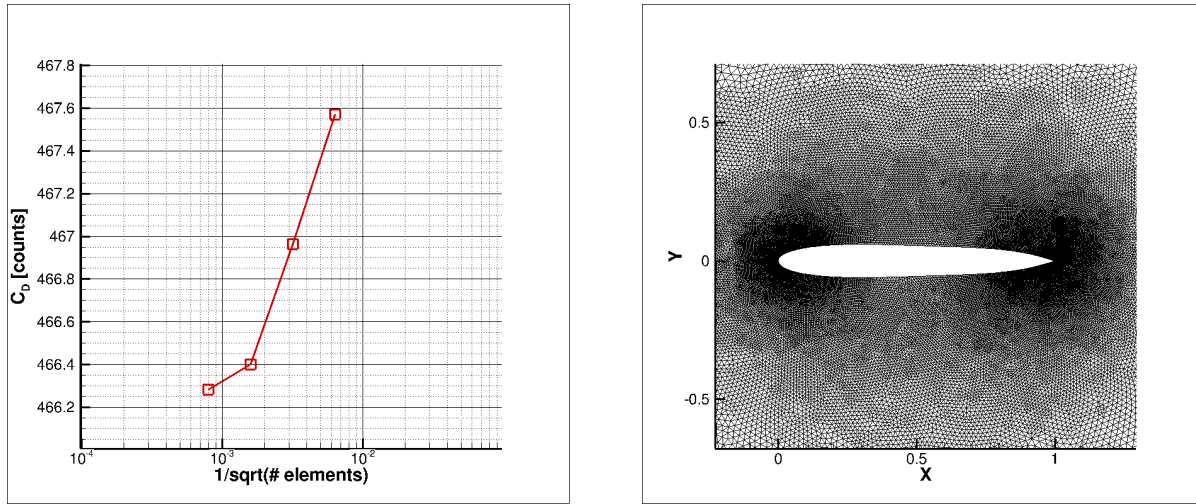
(a) Mesh convergence for the NACA-0012mod airfoil

(b) Mesh distribution around the airfoil for the optimization mesh

Figure 1. Grid convergence (a) and close-up view of the mesh distribution around the airfoil employed during optimization

The resulting pressure distribution is shown in Figure 4. The drag reduction has been achieved by moving the shock downstream 10% of the chord with respect to the baseline airfoil. The drag reduction mechanism exploited (by the current optimization) appears to be the same encountered by other workshop's participants:[13] the optimization algorithm tends to push the shock towards the trailing edge of the airfoil. However, the optimized airfoil drag value is more than 100 drag-counts higher than that from other participants. By looking at the properties on the airfoil surface, Figure 4(a), the leading edge pressure distribution is similar to that of the baseline airfoil as a consequence of the rounded leading edge. The shock has similar intensity as that from other participants.[13] However, it is a long supersonic/subsonic shock that propagates deep into the field hence lacking the short supersonic/supersonic shock seen by other participants and considered to be responsible for the low-drag behavior of those airfoils,[13] as clearly highlighted in Figure 5. The effect of mesh resolution is investigated by analyzing the optimized geometry on the finest mesh from Figure 1(a), consisting of approximately 1.6 million elements. Figure 6(a) shows that the optimized pressure distribution between the optimization mesh and the finest mesh available are similar, while Figure 6(b) confirms the absence of a supersonic/supersonic region after the shock even for the finest mesh.

As shown in Figure 2, partial convergence of the optimization is not responsible for the higher drag experienced by the optimized airfoil. One explanation is certainly the chosen geometry parameterization that enforces a rounded leading edge,[12] while it has been shown[13] that the optimal leading edge tends to be blunt. Another possible justification for this behavior is the enforcement of the thickness constraint, equation (17), that truly results in a condition at all the chordwise coordinates of the airfoil, as compared to enforcing the constraint only at certain chordwise locations as done, for example, in.[14]

III.B. Case 3: Twist optimization of the NACA0012mod wing in inviscid flow

The goal of this optimization is to reduce the (induced) drag of a rectangular wing under a lift constraint. The wing has unit chord and an aspect ratio of $AR = 6$ with a rounded tip-cap at the wing-tip and uses NACA-0012mod airfoil shapes. The optimization problem can be stated as follow

$$min\ C_D$$
$$\texttt{subject to}$$
$$C_L = 0.375 \qquad\qquad (18)$$
$$w.r.t.\ \mathbf{D}$$

where the vector of design variables is composed of the twist values at 5 uniformly spaced spanwise locations as shown in Figure 7. The twist axis is the trailing edge of the wing and the twist between two defining spanwise stations is determined via linear interpolation. The flow is inviscid and the Mach number is $M = 0.5$. This optimization is carried out on a mesh consisting of approximately 440,000 nodes shown in Figure 8. The far field is 40 chords away
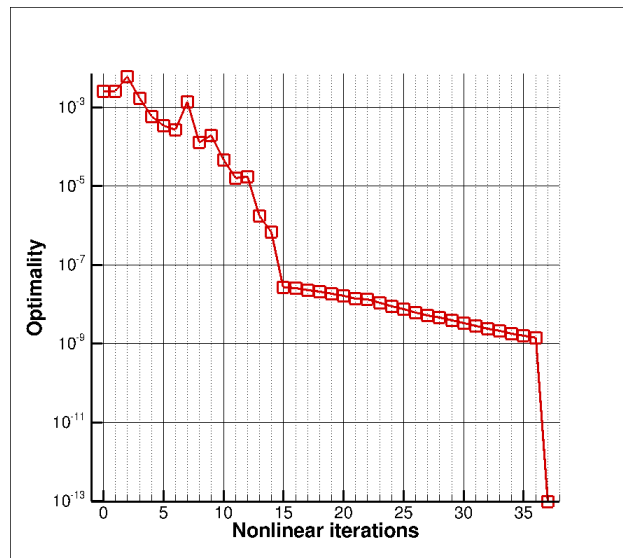
American Institute of Aeronautics and Astronautics

**Figure 2. Optimization convergence for the NACA-0012mod airfoil**

and only half of the wing is simulated with the imposition of a symmetry boundary condition at the root of the wing. On this mesh the baseline wing reaches the target lift of $C_L = 0.375$ at an angle of attack $AOA_{base} \approx 4.39$ deg and has a baseline drag of $C_D = 69.646$ drag-counts. At these conditions the span efficiency factor is $e_{base} = 1.0753$ For the optimization the angle of attack is fixed at the baseline value and the root twist is fixed at zero.

Optimization convergence is shown in Figure 9 highlighting that both feasibility and optimality have dropped several order of magnitudes in just 20 nonlinear iterations. The optimized drag is $C_D = 68.454$ drag-counts, and the span efficiency factor is now $e = 1.0941$. This marginal drag improvement is comparable to optimization results from other workshop's participants.[15–17] The optimal twist distribution is shown in Figure 10 while the wing geometry is presented in Figure 11.

IV.   Conclusion and Future Works

We have presented initial optimization results from the ADODG benchmark problem 1 and 3. Both optimizations have been successful. The two dimensional NACA-0012mod optimization resulted in an airfoil geometry characterized by higher drag levels compared to other workshop's participants. It is believed that the chosen parameterization is responsible for this behavior. The three dimensional optimization is characterized by small drag improvements but results are in good agreement with other participants. Future work will focus on improving the current optimization results and on the remaining benchmark problems.

References

[1]Hicks, R. and Henne, P., "Wing Design by Numerical Optimization," *Journal of Aircraft*, Vol. 15-7, 1978, pp. 407–412.

[2]Jameson, A., "Aerodynamic Shape Optimization using the Adjoint Method," *VKI Lecture Series on Aerodynamic Drag Prediction and Reduction, von Karman Institute of Fluid Dynamics, Rhode St Genese, Belgium*, 2003.

[3]Jameson, A. and Vassberg, J., "Computational Fluid Dynamics for Aerodynamic Design: Its Current and Future Impact," *AIAA Paper 2001–0538*, 2001, Proceedings of the 39th Aerospace Sciences Meeting and Exhibit, Reno NV.

[4]Mavriplis, D. J., "Discrete Adjoint-Based Approach for Optimization Problems on Three-Dimensional Unstructured Meshes," *AIAA Journal*, Vol. 45-4, April 2007, pp. 741–750.

[5]Mavriplis, D. J. and Mani, K., "Unstructured Mesh Solution Techniques using the NSU3D Solver," *AIAA Paper 2014-0081*, 2014, 52nd AIAA Aerospace Sciences Conference.

[6]Mavriplis, D. J., "Unstructured-Mesh Discretizations and Solvers for Computational Aerodynamics," *AIAA Journal*, Vol. 46-6, June 2008, pp. 1281–1298.

[7]Yang, Z. and Mavriplis, D. J., "A Mesh Deformation Strategy Optimized by the Adjoint Method on Unstructured Meshes," *AIAA Journal*, Vol. 45, No. 12, 2007, pp. 2885–2896.

[8]Mavriplis, D. J., Yang, Z., and Long, M., "Results using NSU3D for the first Aeroelastic Prediction Workshop," *AIAA Paper 2013–0786*, 2013, Proceedings of the 51st Aerospace Sciences Meeting and Exhibit, Grapevine TX.

American Institute of Aeronautics and Astronautics
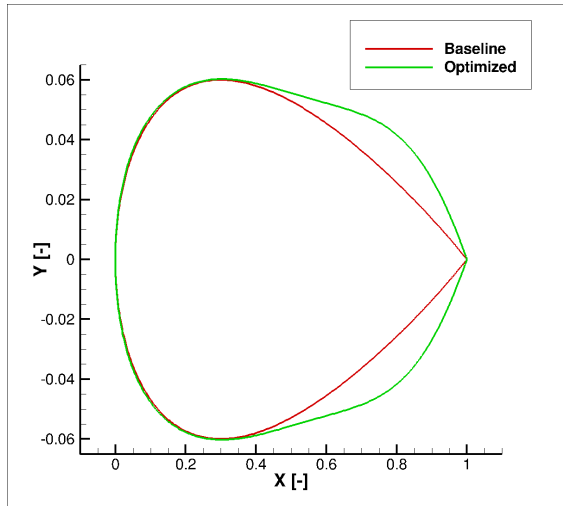
(a) Exaggerated view of the baseline and optimized airfoils
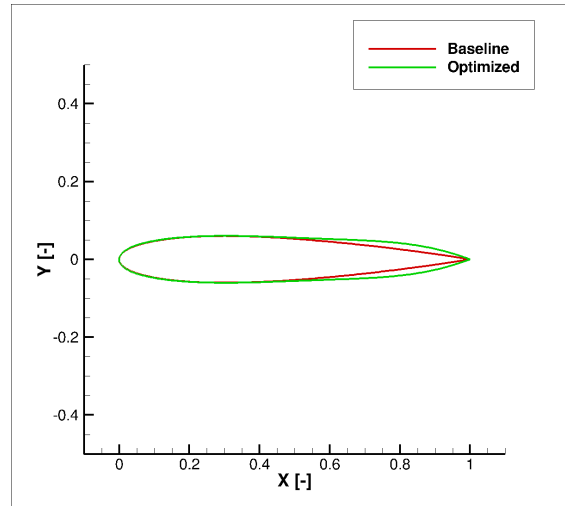
(b) Baseline and optimized airfoil shapes.

Figure 3. Exaggerated (a) and standard (b) views of the airfoil shapes.

[9]Mavriplis, D. J., "Solution of the Unsteady Discrete Adjoint for Three-Dimensional Problems on Dynamically Deforming Unstructured Meshes," *AIAA Paper 2008–0727*, 2008, Proceedings of the 46th Aerospace Sciences Meeting and Exhibit, Reno NV.

[10]Gill, P. E., Murray, W., and Saunders, M. A., "SNOPT: An SQP Algorithm for Large-Scale Constrained Optimization," *SIAM review*, Vol. 47-1, 2005, pp. 99–131.

[11]Vassber, J. C., Harrison, N. A., Roman, D. L., and Jameson, A., "A Systematic Study on the Impact of Dimensionality for a Two-Dimensional Aerodynamic Optimization Model Problem," *AIAA Paper 2011–3176*, June 27–30 2011, 29th AIAA Applied Aerodynamics Conference.

[12]Kulfan, B. M., "Universal Parametric Geometry Representation Method," *Journal of Aircraft*, Vol. 45-1, 2008, pp. 142–158.

[13]Meheut, M., Destarac, D., Carrier, G., Anderson, G., Nadarajah, S., Poole, D., Vassberg, J., and Zingg, W. Z., "Gardient-Based Single and Multi-point Aerodynamic Optimizations with the elsA Software," *AIAA Paper 2015–0263*, January 5–9 2015, 53rd AIAA Aerospace Science Meeting.

[14]Zhang, M., Rizzi, A., and Nangia, R., "Transonic airfoil and Wing Design Using Inverse and Direct Methods," *AIAA Paper 2015-1943*, 2015, 53rd AIAA Aerospace Sciences Meeting.

[15]Bisson, F. and Nadarajah, S., "Adjoint-Based Aerodynamic Optimization of Benchmark Problems," *AIAA Paper 2015–1948*, January 5–9 2015, 53rd AIAA Aerospace Science Meeting.

[16]Lee, C., Telidetzki, K., Buckley, H., Gagnon, H., and Zingg, D. W., "Aerodynamic Shape Optimization of Benchmark Problems Using Jetstream," *AIAA Paper 2015-0262*, January 2015, 53rd AIAA Aerospace Sciences Meeting, Kissimmee, Fl.

[17]Anderson, G. R., Nemec, M., and Aftosmis, M. J., "Aerodynamic Shape Optimization Benchmarks with Error Control and Automatic Parameterization," *AIAA Paper 2015–1719*, January 5–9 2015, 53rd AIAA Aerospace Science Meeting.

American Institute of Aeronautics and Astronautics
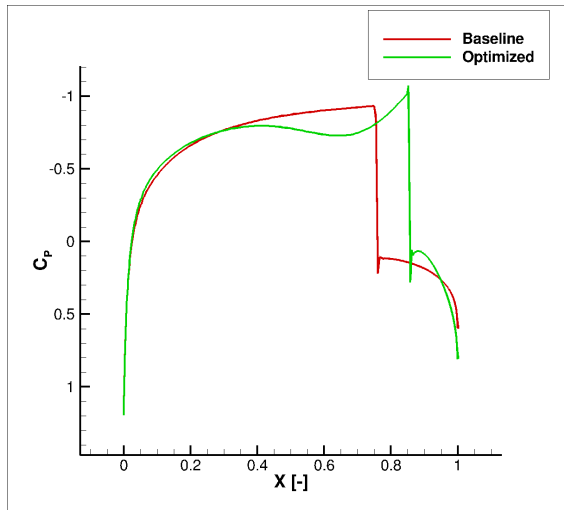
(a) Baseline and optimized pressure coefficients.
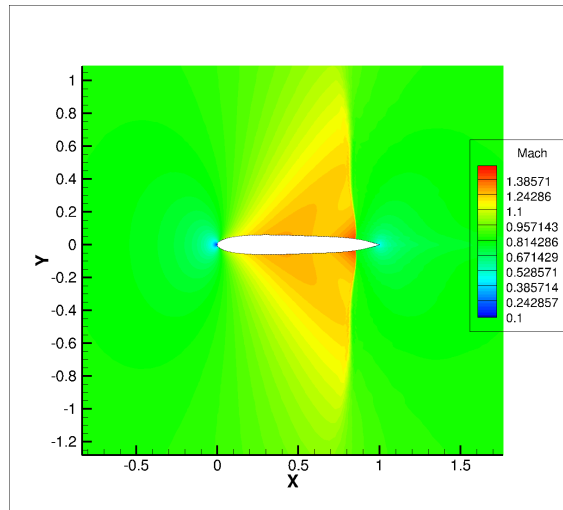
(b) Mach contours for the optimized airfoil.

Figure 4. Baseline and optimized pressure distributions (a) and optimized airfoil Mach number contours (b)
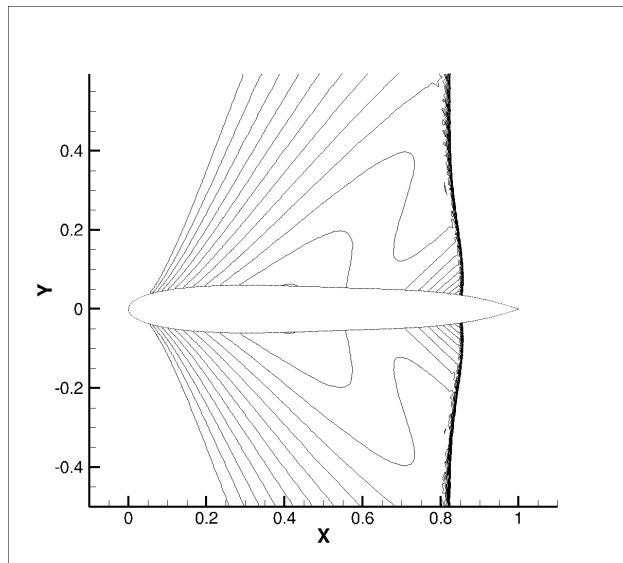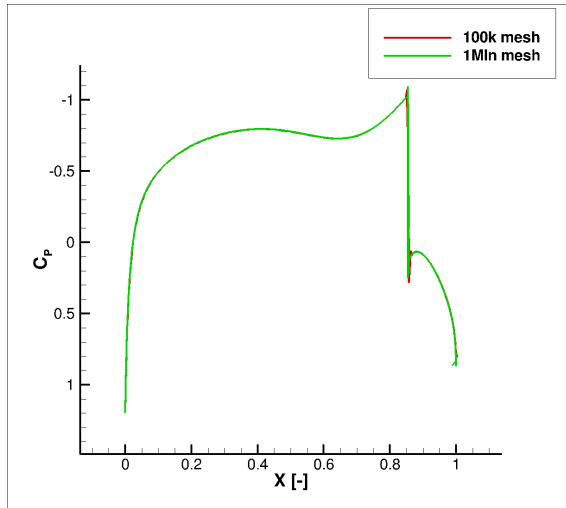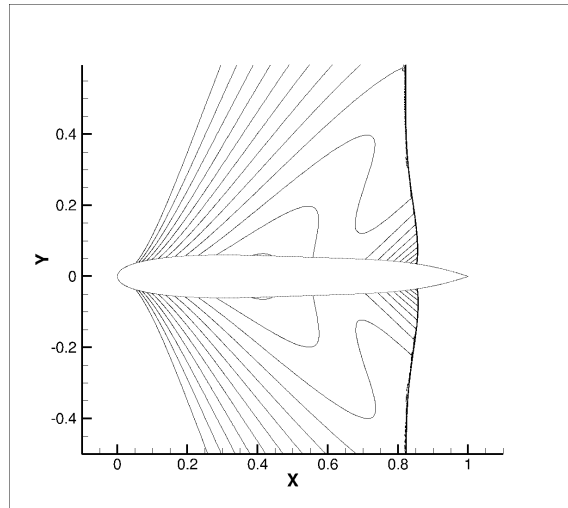

Figure 5. Supersonic iso-Mach number lines with $\Delta M = 0.025$ showing the absence of a supersonic/supersonic region right after the shock for the optimized airfoil.

American Institute of Aeronautics and Astronautics

(a) Pressure distribution comparison between the 100,000 elements and the 1.6 million elements mesh.

(b) Supersonic iso-Mach number lines with $\Delta M = 0.025$ for the 1.6 million elements mesh showing again the absence of a supersonic/supersonic region right after the shock for the optimized airfoil.

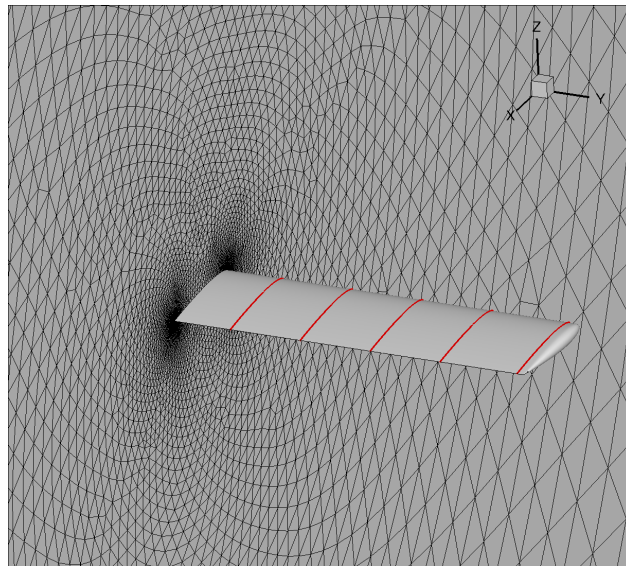**Figure 6. Surface pressure and flowfield results from the 1.6 million element mesh.**

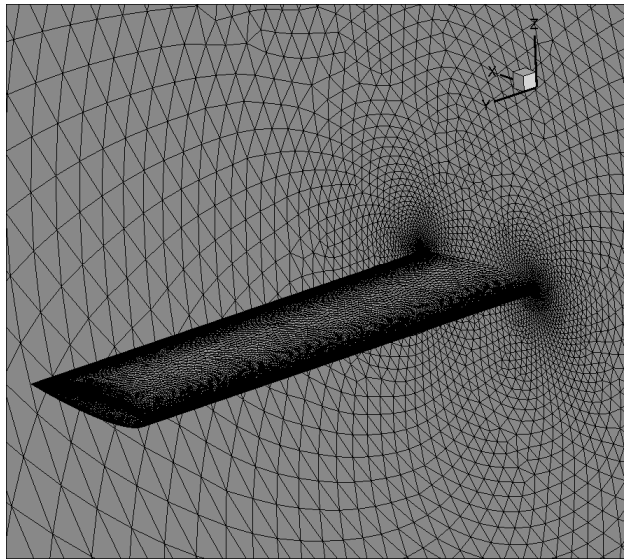**Figure 7. Geometry parameterization for the NACA-0012mod rectangular wing. Twist stations are highlighted in red.**

American Institute of Aeronautics and Astronautics

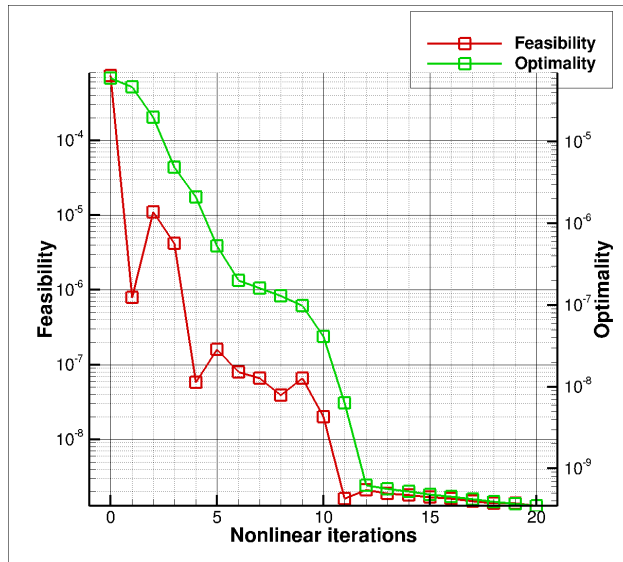**Figure 8. Details of the computational mesh around the NACA-0012mod rectangular wing.**

Figure 9. Optimization convergence for the NACA-0012mod wing

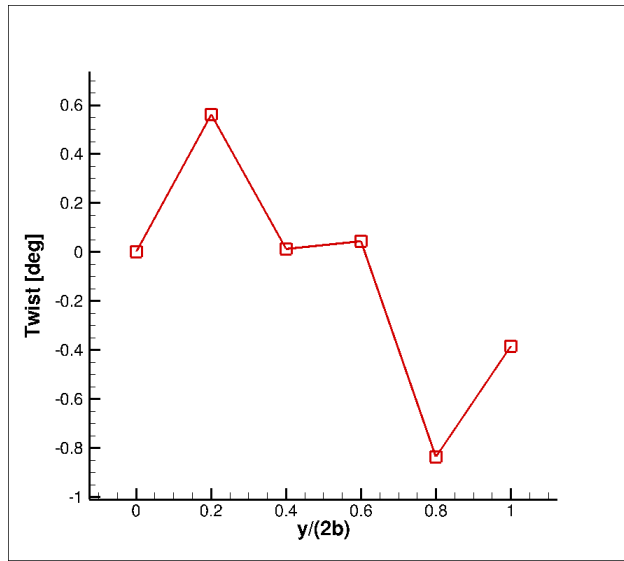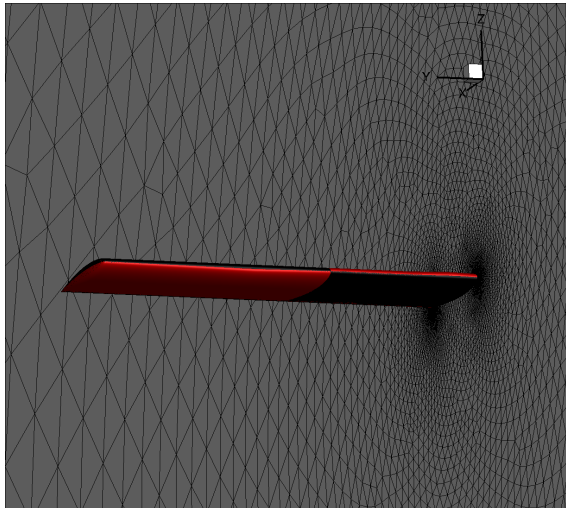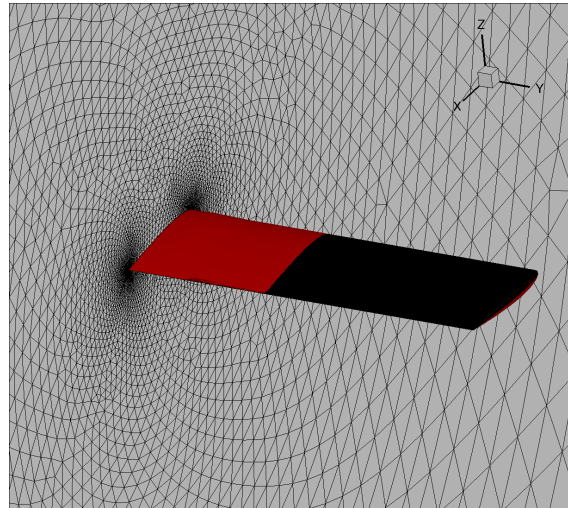American Institute of Aeronautics and Astronautics

Figure 10. Optimal twist distribution for the NACA-0012mod wing

(a) Front view of the baseline (black) and optimized (red) wing geometries.

(b) Back view of the baseline (black) and optimized (red) wing geometries.

Figure 11. Baseline and optimized wing geometries.

American Institute of Aeronautics and Astronautics